Reconstruction of multi-animal PET acquisitions with anisotropically variant PSF

F. Arias-Valcayo[1], **P. Galve**[1,2,3], **Joaquín L. Herraiz**[1,2], **J. J. Vaquero**[4,5], **M. Desco**[4,5,6,7], **J.M. Udías**[1,2]

[1] Grupo de Física Nuclear, EMFTEL & IPARCOS, Universidad Complutense de Madrid, CEI Moncloa, Madrid, Spain

[2] Instituto de Investigación Del Hospital Clínico San Carlos (IdISSC), Ciudad Universitaria, Madrid, Spain

[3] Universite Paris Cite, PARCC, INSERM 56, rue Leblanc Paris, Île-de-France, FR

[4] Departmento de Bioingeniería, Universidad Carlos III de Madrid, Madrid, Spain

[5] Instituto de Investigación Sanitaria Gregorio Maranón, Madrid, Spain

[6] Centro Nacional de Investigaciones Cardiovasculares Carlos III (CNIC), Madrid, Spain

[7] CIBER de Salud Mental, Instituto de Salud Carlos III. Madrid, Spain

E-mail: `farias02@ucm.es`

Abstract. Among other factors such as random, attenuation and scatter corrections, uniform spatial resolution is key to performing accurate quantitative studies in Positron emission tomography (PET). Particularly in preclinical PET studies involving simultaneous acquisition of multiple animals, the degradation of image resolution due to the depth of interaction (DOI) effect far from the center of the Field of View (FOV) becomes a significant concern. In this work, we incorporated a spatially-variant resolution model into a real time iterative reconstruction code to obtain accurate images of multi-animal acquisition. We estimated the spatially variant point spread function (SV-PSF) across the FOV using measurements and Monte Carlo (MC) simulations. The SV-PSF obtained was implemented in a GPU-based Ordered subset expectation maximization (OSEM) reconstruction code, which includes scatter, attenuation and random corrections. The method was evaluated with acquisitions from two preclinical PET/CT scanners of the SEDECAL Argus family: a Derenzo phantom placed 2 cm off center in the 4R-SuperArgus, and a multi-animal study with 4 mice in the 6R-SuperArgus. The SV-PSF reconstructions showed uniform spatial resolution without significant increase in reconstruction time, with superior image quality compared to the uniform PSF model.

Keywords: PSF, real-time, Positron Emission Tomography, GPU

1. Introduction

Preclinical positron emission tomography (PET) scanners with extended Field of View (FOV) offer the capability to image multiple animals simultaneously, leading to cost reduction and enhanced radiotracer efficiency [1, 2]. Due to the fact that the animals may be placed far from the center of the field of view (FOV), uniform image resolution and general image quality across the FOV is paramount [3, 4, 5, 6]. This work proposes an algorithm to improve the resolution uniformity of reconstructed images, enabling multi-animal imaging.

Iterative methods in PET image reconstruction with resolution modeling in the system response matrix (SRM) achieve improved spatial resolution and signal-to-noise ratio [7, 8, 9, 10]. Iterative reconstructions can model the most relevant physical effects during emission, transport and detection of the radiation [11, 12]. Point Spread Function (PSF) models, implemented in the SRM using image or projection blurring kernels, are commonly used to achieve resolution modeling [13, 14, 15]. Often, a symmetric Gaussian PSF with uniform characteristics across the scanner's FOV is employed for simplicity [16]. However, more realistic models that account for spatially variant PSFs have been proposed [17, 18], yielding favorable results in both clinical [19] and preclinical studies [20]. Spatially variant PSFs has shown an improvement in spatial resolution and thus quantification in the whole FOV, enabling simultaneous scanning of multiple animals without compromising quantitative accuracy [21].

There are different approaches to obtain a realistic PSF resolution model: 1) By using experimental measurements of point sources at various locations throughout the scanner FOV and parameterizing the observed PSF dependence on position [22, 23]. 2) By employing Monte Carlo simulations and analytical computations to estimate the PSF along the FOV [24, 25].

Resolution modeling through PSF convolution using a kernel in the image domain, despite being an approximation, has demonstrated the ability to produce high-quality images [26]. This approach offers the advantage of easy implementation in list-mode iterative Maximum Likelihood Expectation Maximization (MLEM) algorithms, making it highly efficient for GPU-based codes [27]. GPUs [28] have successfully addressed concerns regarding increased reconstruction time associated with resolution recovery methods. Pratx et al. [16] efficiently modeled scanner resolution using fixed-width Gaussian kernels on GPUs. In our work, we introduce kernels of varying sizes in each direction to account for non-uniform resolution across the FOV in numerous scanners. Recent studies have demonstrated that GPU acceleration translates into enhanced clinical workflows and even real-time PET imaging capabilities [29].

PSF can be modeled with different levels of complexity and accuracy. The simplest model is a uniform symmetric PSF that takes into account the average of certain physical effects such as detector size, positron range, and non-collinearity. In other works [20], radial asymmetry was considered into the PSF calculation, but the axial dependency was not considered. Our work aims to generalize the PSF by allowing spatial variability in all directions, thereby considering the anisotropy of the scanner across the FOV. We have develop a workflow that estimates the PSF through a simulation of a grid of point sources within the FOV. We considered two scanners of the SEDECAL Argus family of microPET/CT preclinical scanners in the context of real-time imaging. We have successfully adapted spatially variant kernels for use in a GPU Ordered Subset Expectation Maximization (OSEM) reconstruction. We further validated our approach through several studies, demonstrating that we achieve a more homogeneous resolution across the entire FOV of the scanner compared to when a fixed PSF is employed. On one hand, we conducted simulations involving point sources covering a large part of the FOV, and on the other hand, we evaluated our method using an off-centered Derenzo phantom [30] acquisition and a multi-animal acquisition involving four mice.

2. Methods

2.1. Scanners

We have evaluated the spatially variant PSF reconstruction in the 4R-SuperArgus and the 6R-SuperArgus scanner [31]. The scanners are composed of two layered blocks of pixellated arrays of 13x13 crystals each of 1.55 mm crystal pitch. A layer of lutetium-yttrium orthosilicate (LYSO) crystals of 7 mm length in the front of the detector is optically coupled to cerium-doped gadolinium orthosilicate (GSO) crystals of 8 mm length in the back. The 4R-SuperArgus is composed of 4 rings of 24 detectors each, with a radial FOV of 17 cm and axial FOV of 11 cm, while the 6R-SuperArgus scanner has 6 rings extending the axial FOV to 15 cm.

2.2. Image reconstruction model

In this work, we have implemented the OSEM algorithm [32] adapted to list-mode data with the SRM factorized in a geometrical projector and a convolutional matrix representing the PSF [13]. The algorithm reads as follows:

$$x_j^{n+1} = x_j^n \left(\frac{G \otimes \sum_{i \in S_k} \mu_i a_{ij} \dfrac{1}{\sum_v \mu_i a_{iv} (G \otimes x_v^n) + s_i + r_i}}{G \otimes \sum_{i \in S_k} \mu_i a_{ij}} \right) \tag{1}$$

Where x_j^n represents the estimated activity of voxel j at iteration n, a_{ij} denotes the geometrical projector element relating the detection probability from voxel j to a LOR i and S_k refers to the LORs within a subset k. The attenuation correction factor (μ_i) is derived from the μ-map obtained from a CT scan. The random (r_i) and scatter correction (s_i) are additive factors accounted in the projection [33]. For acquisition of mice and phantoms, besides attenuation derived from a micro-CT, randoms are taken from the information of the scanner in the list-mode data, and scatter is estimated at every iteration in the reconstruction from an ultra fast Monte Carlo (MC) simulation given the CT and the activity of the previous iteration. For simulations and acquisitions of point sources, as they have almost no additional material, attenuation and scatter corrections were negligible. The blurring kernel (G) accounts for the PSF of the imaging system. We convolve the image with the PSF prior to the forward projection operation, and after the backward projection operation. The reconstruction software is implemented using the PGI CUDA Fortran Compiler [34].

2.3. Parametrization of spatially invariant PSF

In this work, we parametrize the PSF by means of gaussian-like shape along the radial (r), tangential (t) and axial (z) directions. To exploit the cylindrical symmetry of the scanners, we assume independent PSF for the transverse plane and the axial axis. Thus, we factorize the PSF with a kernel representing the radial and tangential PSF and a kernel with the axial PSF (figure 1).

The image element x_j is convoluted with the kernel G, resulting in the image element x'_j as follows:

$$x'_j = G \otimes x_j = \sum_{v \in \varphi} g_{j-v}(r_{j-v}, z_{j-v}) x_v \tag{2}$$

Where $g_j(r_j, z_j)$ is the element j of the blurring kernel G, and r_j and z_j are the radial and axial positions of voxel j inside the scanner. It is important to remark that r_j and z_j do not represent the relative distance from voxel j to voxel v in 2. φ is a 3D region around the voxel j (in this work we have used a 31×31×31 region).

The elements $g_j(r_j, z_j)$ are factorized in two separate kernels as:

$$g_j(r_j, z_j) = N_j g_j^z(r_j, z_j) g_j^{t,r}(r_j, z_j) \tag{3}$$

$$N_j = \frac{1}{\sum_{j \in \varphi} g_j^z(r_j, z_j) g_j^{t,r}(r_j, z_j)} \tag{4}$$

Where N_j is a normalization factor, $g_j^z(r_j, z_j)$ describes the axial kernel, and $g_j^{t,r}(r_j, z_j)$ describes the tangential-radial kernel:

$$g_j^z = e^{\frac{-dz_j^2}{2\sigma_z^2(r_j, z_j)}} \tag{5}$$

$$g_j^{t,r} = e^{\frac{-dr_j^2}{2\sigma_r^2(r_j, z_j)}} \times e^{\frac{-dt_j^2}{2\sigma_t^2(r_j, z_j)}} \tag{6}$$

Where dz_j, dr_j and dt_j are the relative distances between the voxels j and v in the convolution, in the axial, radial, and tangential axes respectively. The parameterization

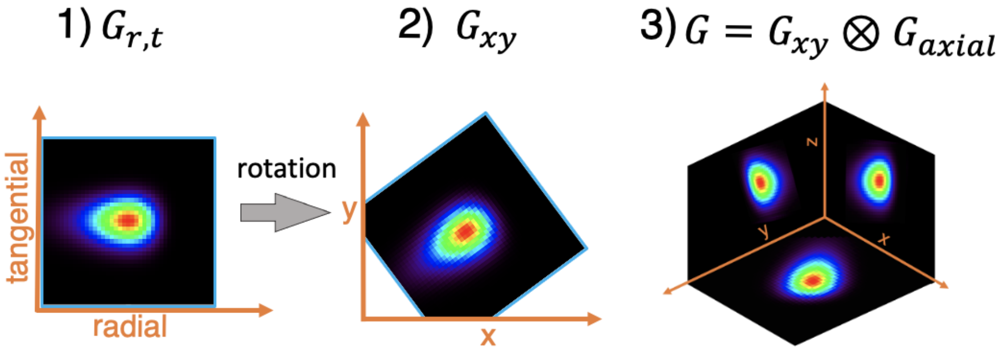

Figure 1: Computation of G kernel. Each thread computes the kernel of each image voxel, and rotates it to map the position of the kernel into the intrinsic cartesian axes of the image. Then, this kernel is combined with the axial kernel.

is introduced by $\sigma_r(r_j, z_j)$, $\sigma_t(r_j, z_j)$ and $\sigma_z(r_j, z_j)$, which depend on the radial and axial position of voxel j. Our approach to parameterizing the PSF enables the incorporation of asymmetric profiles in all directions (axial, radial, tangential) (see figure 1 displaying the PSF profiles in these three directions), extending previous PSF-based SRM modeling.

We implemented the computation and application of the G kernel in GPU. Each thread of the GPU calculates the kernel for a voxel (figure 1). In order to simplify the calculation, we first obtain the 2D Gaussian kernel of the tangential-radial plane, and after that we apply the rotation needed to match the voxel position in the cartesian grid:

$$\begin{bmatrix} x' \\ y' \end{bmatrix} = \begin{bmatrix} \cos\theta & -\sin\theta \\ \sin\theta & \cos\theta \end{bmatrix} \begin{bmatrix} x \\ y \end{bmatrix} \qquad \theta = \arctan\frac{y}{x} \tag{7}$$

$$G = G_{xy} \otimes G_{axial} = R_\theta G_{r,t} \otimes G_{axial} \tag{8}$$

To obtain the parametrization of $\sigma_r(r, z)$, $\sigma_t(r, z)$ and $\sigma_z(r, z)$, a grid of point sources across the FOV of the scanner was simulated. For the 6R-SuperArgus we simulated point sources from radius 0 cm to 8.5 cm in steps of 0.5 cm and from $z = 0$ cm to $z = 7.2$ cm in steps of 0.4 cm (figure 2). For the 4R-SuperArgus, we have simulated point sources from radius 0 to 8.5 cm and from z = 0 cm to z = 4.8 cm. We reconstructed the image from the simulated point sources, without PSF modeling, which would represent the point source blurred with the intrinsic scanner resolution. We fit every source of this image to obtain the $\sigma_r(r, z)$, $\sigma_t(r, z)$ and $\sigma_z(r, z)$ parameters across the FOV of the scanner. For this procedure, we have reconstructed images with small voxel size of $0.2 \times 0.2 \times 0.2$ mm^3 and 5 iterations, since without resolution modeling, we have verified that increasing the number of iteration only increase the noise and the shape of the source remains fixed. During reconstruction, every $\sigma(r, z)$ is calculated by cubic spline interpolation.

As shown in figure 2, the blurring of the image of the sources along the radial direction is different for every axial position. For this reason, it is necessary to consider

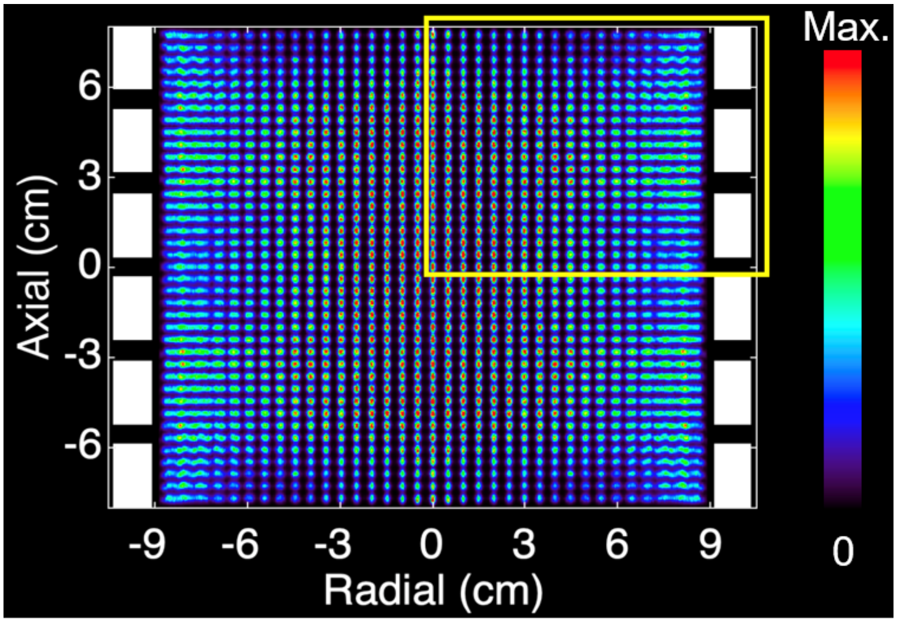

Figure 2: Reconstructed images, without resolution recovering, that is, with no PSF, of the point sources simulated across the full FOV of the 6R-SuperArgus scanner (central plane shown). The size and shape of these images represents the PSF in each case. Thanks to symmetries only one quadrant needs to be simulated and parametrized (yellow box). Scanner detectors are also represented in the figure in white.

the shape and size of the PSF in both the radial and z coordinates.

2.4. Monte Carlo reconstruction

We have compared the PSF iterative reconstructions with a full Monte Carlo (MC) [35] reconstruction, which will be considered the gold standard reference. We will briefly describe the MC reconstruction. First, a large list of events, that is, voxel of emission and LOR of detection pairs, is generated using a MC simulation which accounts for the most relevant physical processes involved. Secondly, the projection step of the OSEM is performed running through the list built during step one, by adding the activity image obtained during the previous iteration for each voxel connected to a given LOR. The backprojection is computed using the same scheme, but instead we add up the correction factors for each LOR (number of coincidences detected in the LOR divided by the estimated activity in the projection) on the image connected to a given voxel. In this way, the MC simulations is employed to introduce resolution recovery in the iterative reconstruction, without any approximation to the geometry or the physics of the problem. Even though it is based on a very fast MC simulation, these reconstructions are very time consuming and therefore their practical use is limited, but here we use them as a reference to confirm that the relevant blurring effects are effectively taken into account by the PSF-based modelling.

2.5. Simulated cases and acquisitions

To test that our parameterized PSF can reproduce the behavior observed in real data, a point source (less than 0.5 mm diameter encapsulated in a 3x3 mm diameter small epoxy cylinder) of ^{22}Na of 5 μCi was placed on the bed of the scanner. A list-mode data acquisition was started while the source was displaced in a step and shoot fashion every 5 mm in a given direction. The list file was afterwards processed to separate the sections corresponding to every position of the point source.

To validate the accuracy of our SV-PSF model, a set of point sources placed every 5 mm along the radial axis have been simulated. Each point source has 10^9 emissions.

We have evaluated the spatially variant PSF reconstruction method in the 4R-SuperArgus with an acquisition of a Derenzo phantom placed 2 cm off center [36] filled with ^{18}F, the initial activity was 250 μCi, and the acquisition took 20 minutes. The reconstructions method were also evaluated with data from a multi-animal study with four mice injected with 572, 569, 562 and 566 μCi of ^{18}F-FDG respectively, acquired simultaneously for 10 minutes in the 6R-SuperArgus scanner. All experimental procedures have been done in compliance with the European Communities Council Directive 2010/63/EU and submitted for approval by the Institutional Animal Care and Use and Ethics Committee of the Hospital General Universitario Gregorio Marañón (HGUGM), supervised by the Comunidad de Madrid according to the Annex X of the RD 53/2013. The subjects were kept at the animal housing facilities of the Unidad de Medicina y Cirugía Experimental (UMCE-HGUGM) in Madrid, Spain.

3. Results

3.1. PSF parametrization

We have compared the image reconstructed from simulated and real point sources at different positions within the FOV of the the 6R-SuperArgus Scanner. In table 1 we show the FWHM for the images of the sources obtained from a fit to the gaussian parametrization. Te maximum discrepancy between the FWHM obtained from simulated and real points is less than 5%, coming mostly from statistical noise in the simulations and acquisitions. This indicates that the simulations are realistic enough to describe the variation of the intrinsic resolution of the scanner in the FOV. Thus, we prepare a dense grid of simulated point sources, and use the image reconstructed from these simulations to fit the parametrization proposed in in this work. In figure 3, we also show the cross-section in the transaxial plane of the images of experimental point sources and the corresponding fitted PSF using the parametrization described in eqations 5 and 6. We see that the parameterized PSF reproduces the behavior observed in real data, including shape and size changes in different regions of the FOV.

In figure 2, we can see that the intrinsic resolution of the scanner, as seen in the reconstructed images of point sources without resolution recovery, exhibits, as expected, a clear degradation with increasing radial distance, which further depends on the axial

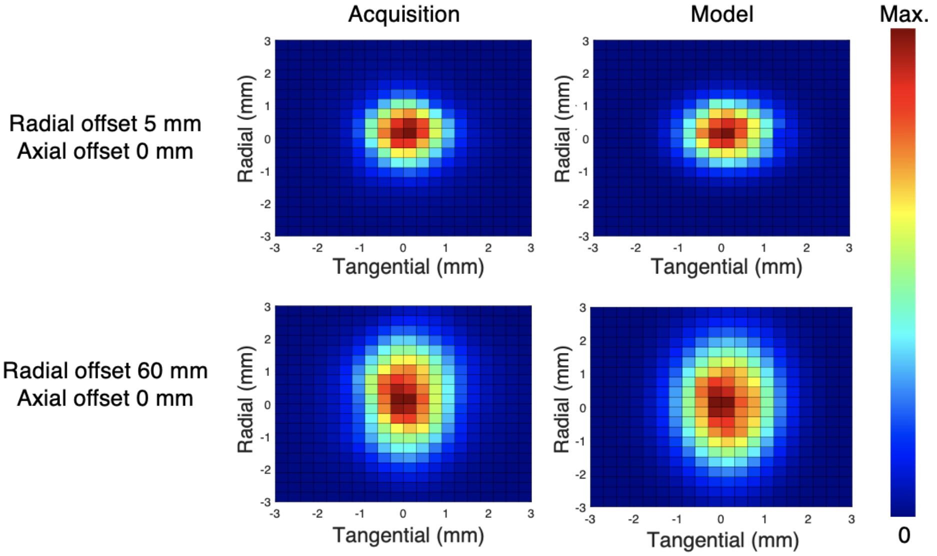

Figure 3: Cross-section in the trans-axial plane of the reconstructed image of the experimental point sources (left) and simulated ones, at 5 mm (top) and 60 mm (bottom) radial offset.

Offset (mm)	Radial FWHM (mm) Simulation	 Acquisition	Tangential FWHM (mm) Simulation	 Acquisition	Axial FWHM (mm) Simulation	 Acquisition
Radial = 0 Axial = 0	1.41	1.51	1.46	1.40	1.21	1.29
Radial = 35 Axial = 0	2.03	2.06	1.71	1.76	1.48	1.50
Radial = 50 Axial = 0	2.35	2.38	1.95	1.89	1.60	1.60
Radial = 5 Axial = 40	1.90	1.98	1.37	1.37	1.71	1.79

Table 1: Comparison of the FWHM obtained by fitting to no resolution recovery iterative reconstructed images of simulated and real point sources at different positions in the FOV of the 6R-SuperArgus scanner. Statistical errors in the fit are below 4% in all cases.

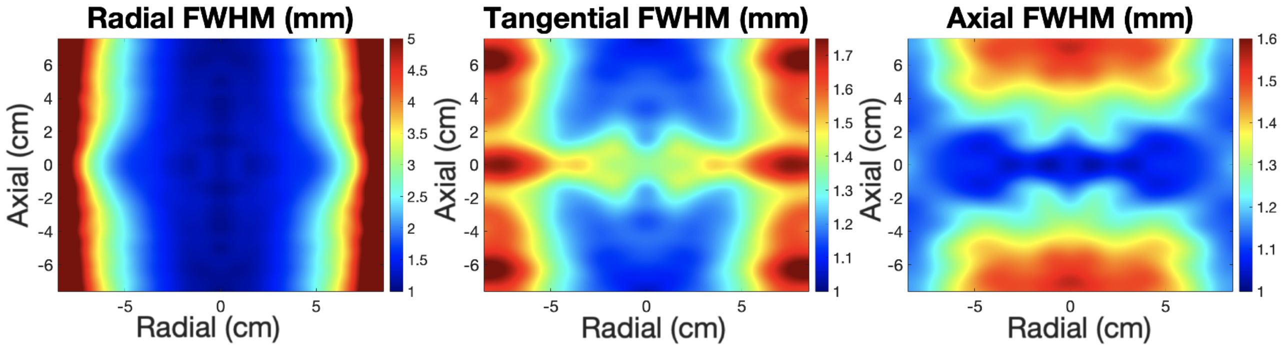

Figure 4: Maps of intrinsic resolution of the scanner as given by the FWHM of the reconstructed point sources in the whole FOV of 6R-SuperArgus scanner.

position, particularly near the border of the FOV, owing to the gap in between detector rings. Our simulations of a grid of point sources allow to produce 3D resolution maps as shown in figure 4 showing the non-uniformity of the intrinsic resolution across the FOV of the 6R-SuperArgus. The same study has been done for the 4R-SuperArgus scanner.

Although the SuperArgus system consists of rings made of 24 detector blocks, the size and shape of the PSFs exhibits to a good approximation cylindrical symmetry. Indeed, we have compared simulated sources in the radial axis at the center of a block, and at the vertex in between adjacent blocks, that is, at $\phi = 7.5$. The reconstruction of these sources without resolution recovery is shown in figure 5. The same figure shows the parameterized FWHM for each case. The maximum difference of FWHM fit to images of corresponding sources at both lines is less than 4%.

3.2. Validation of the approach: Reconstruction of Point Sources

Once the spatially variant PSF has been determined, it can be incorporated into the iterative reconstruction process. In order to evaluate the performance of our method, we conducted a comparative analysis using images of a set of point sources placed at 5 mm intervals along the radial axis, under two different scenarios.

In the first scenario, which represents typical conditions for preclinical animal acquisitions with controlled statistics, we employed $5 \cdot 10^8$ emissions per source, voxel dimensions of 0.33 mm^3, and performed 6 iterations with 5 subsets. This would be representative of typical animal acquisitions with FDG, which are limited by the amount of tracer that can be injected in mice, and the reasonable scanning time. In the second scenario, our objective was to investigate the resolution limits of our method. Thus, we simulated with larger emission count of 10^{11} per source, utilized smaller voxel sizes of 0.15 mm^3, and performed 50 iterations with 5 subsets. This would correspond to optimal conditions for high statistics acquisitions.

For the first scenario, we compared three different reconstruction methods: MC reconstruction, reconstruction using a fixed PSF (with dimensions of 1.4x1.4x1.7 mm,

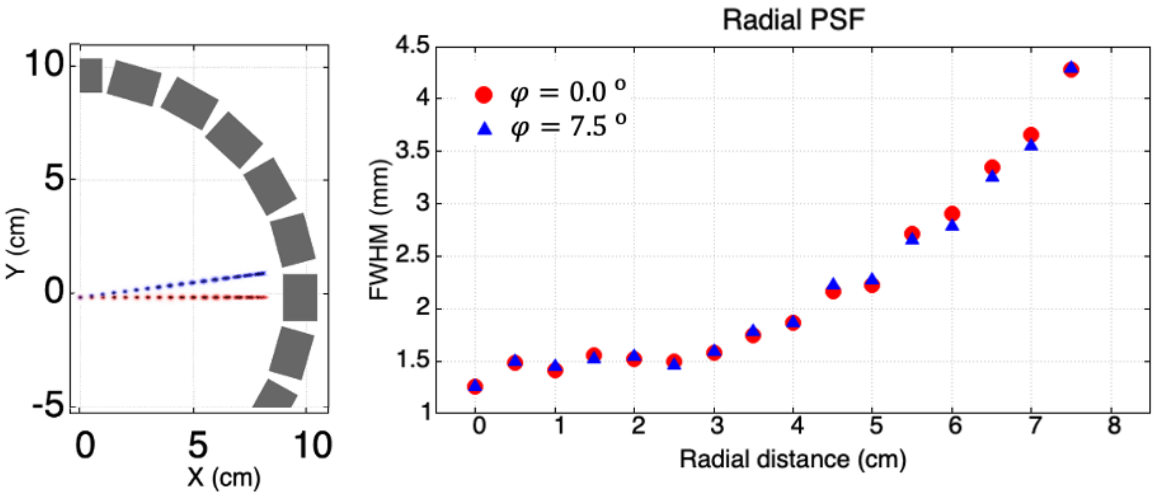

Figure 5: Left: point sources reconstructions without resolution recovery for a radial axis ending in the middle of a detector block (red) and for a radial axis ending in a gap between two detectors (blue). Right: FWHMs along the radial axis for these sources are shown.

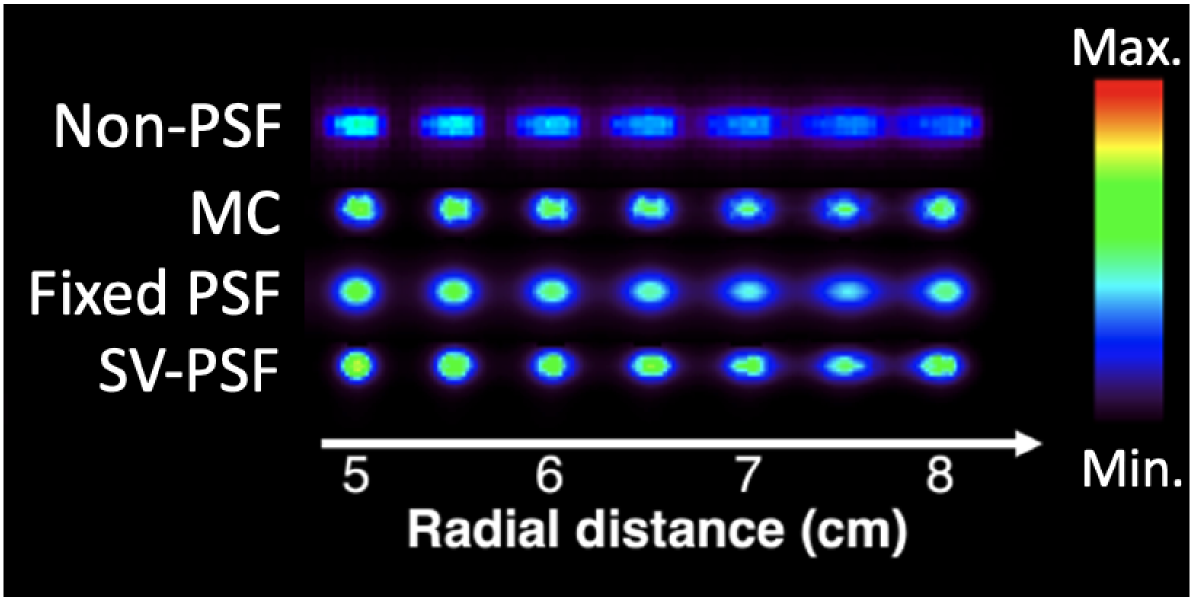

Figure 6: Reconstruction from simulated point sources in the 6R-SuperArgus reconstructed with non-PSF, the Monte Carlo method, the fixed PSF (1.4x1.4x1.7 mm^3) and the SV-PSF. All reconstructions have 6 iterations 5 subsets and voxel size of 0.33 mm^3.

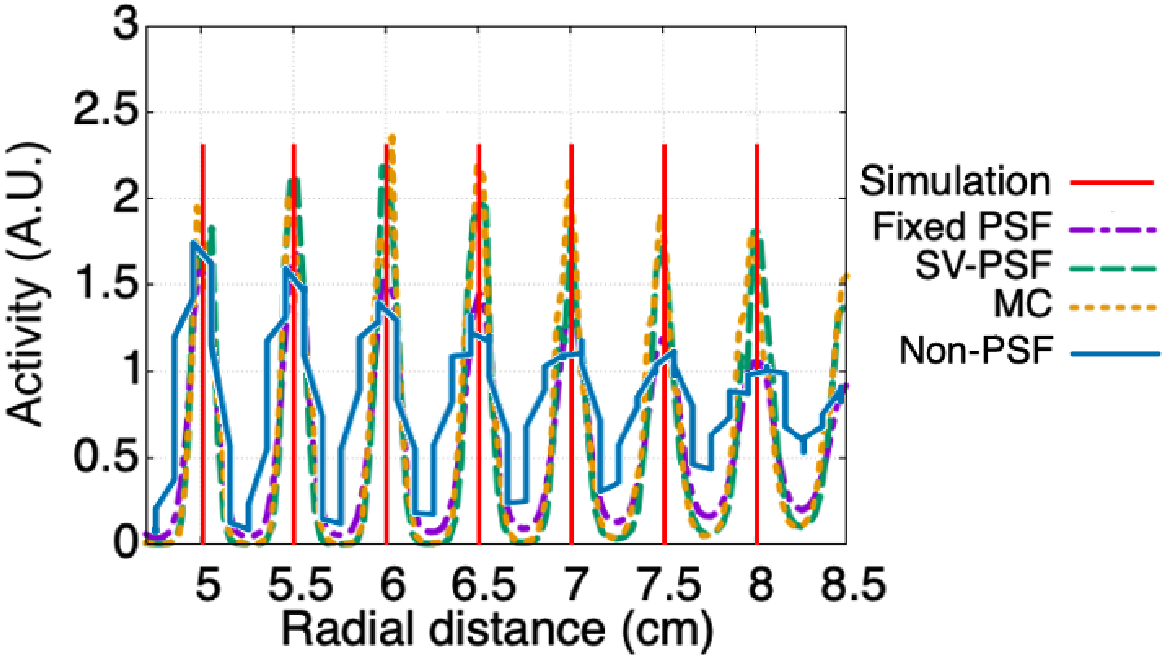

Figure 7: Radial profile of reconstructed images of simulated point sources, obtained with non-PSF, Monte Carlo reconstruction, fixed PSF (1.4x1.4x1.7 mm^3) and the proposed SV-PSF in the 6R-SuperArgus. In red, the position of the sources simulated.

representing the average PSF in the vicinity of the scanner's center, where higher resolution is typically desired), and reconstruction using the SV-PSF model obtained through our parameterization approach. Figure 6 depicts the reconstructed images of the point sources located further from the center using the three different reconstruction methods. Additionally, figure 7 displays the profile along these sources, providing further evidence of the comparable resolution between SV-PSF and MC reconstructions. These results demonstrate the effectiveness of the SV-PSF model in recovering high-resolution details at the same level as the MC reconstruction.

For the second scenario we compare just fixed PSF versus SV-PSF reconstructions. Figure 8 presents the FWHM measurements obtained from the reconstructed images of the point sources in both scenarios, considering the radial, tangential, and axial directions. In the first scenario, represented at the top of the image, under standard conditions, the radial FWHM demonstrates the largest variation due to the depth of interaction. However, this variation is significantly reduced in both the MC and SV-PSF reconstructions. Overall, in each direction, the SV-PSF reconstruction exhibits a resolution improvement that closely approaches the performance of the reference MC method. showing that the SV-PSF iterative reconstruction as parameterized in this work is able to incorporate the blurring effects introduced in the simulations very efficiently.

For this second scenario, displayed at the bottom of the figure 8, a similar trend is observed. The SV-PSF reconstruction consistently achieves better resolution across all cases. Notably, for the SV-PSF method, resolutions below 1 mm are attained up to a distance of 5 cm from the center of the scanner, whereas the Fixed-PSF reconstruction only achieves sub-1 mm resolution up to approximately 2.5 cm. This significant improvement in resolution highlights the superior performance of the SV-PSF approach in capturing fine details even far from the center of the imaging system.

3.3. Derenzo Acquisition

Figure 9 presents a comparison between Fixed PSF and SV-PSF reconstructions based on a real acquisition of a 2 cm off-center Derenzo phantom in 4R-SuperArgus. Both reconstructions were stopped at the same noise level, achieved through 5 subsets and 15 iterations for SV-PSF, and 5 subsets and 12 iterations for fixed PSF, as demonstrated in figure 10. Specifically, both reconstructions were halted when reaching a noise level of 7.5%. The noise level was quantified within a region of interest (ROI) exhibiting homogeneous activity and calculated as the standard deviation of the ROI divided by its mean value.

Remarkably, the SV-PSF model exhibited an average improvement of 8% in FWHM for the 1.6 mm rods compared to the Fixed PSF method. Furthermore, for the 3 mm rods located farther from the center, the SV-PSF model demonstrated a reduction of 23% in FWHM. This notable enhancement can be attributed to the SV-PSF model's superior ability to handle the off-center positioning of these rods, resulting in improved reconstruction accuracy and finer spatial resolution.

3.4. Multianimal Acquisition

Figure 11 shows the reconstruction of four mice acquired in the 6R-SuperArgus scanner spanning 8 cm of trans-axial FOV.

	PV ratio	
Mouse	PV Fixed PSF	PV SV-PSF
1	3.86	5.97
2	2.79	3.52
3	2.64	3.91
4	4.10	6.02

Table 2: Comparison of peak-to-valley ratios (PV) for each mouse heart with fixed PSF and SV-PSF. PV is computed as the ratio of the maximum intensity within the myocardium to the minimum intensity within the same region. This metric is obtained from the profiles shown in Figure 12. Higher resolution leads to increased PV ratios

Figure 12 shows a close-up of the heart of each mouse, using either the fixed PSF or the SV-PSF. We recall that the reconstructions were stopped at the same noise level in

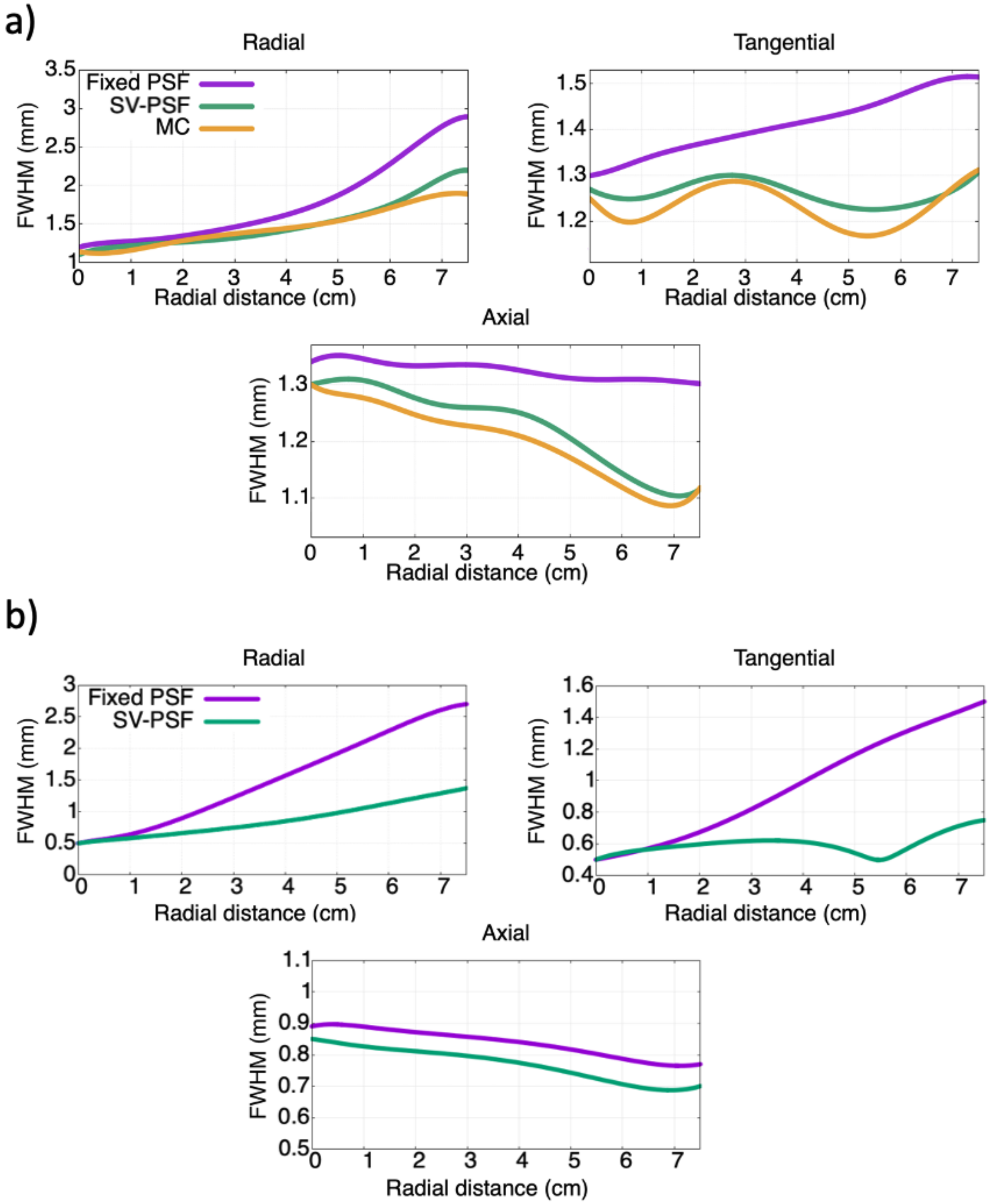

Figure 8: FWHM in the radial, tangential, and axial directions of reconstructed images obtained from acquisitions of simulated point sources using the 6R-SuperArgus scanner. The figure presents results for two different scenarios: a) at the top, utilizing $5 \cdot 10^8$ emissions per source, 6 iterations, 5 subsets, and a voxel size of 0.33 mm^3. The reconstructions were performed using the MC method, the Fixed-PSF (1.4x1.4x1.7 mm^3), and the SV-PSF. b) At the bottom, employing 10^{11} emissions per source, 50 iterations, 5 subsets, and a voxel size of 0.15 mm^3. In this case, only the Fixed-PSF and SV-PSF reconstructions are shown.

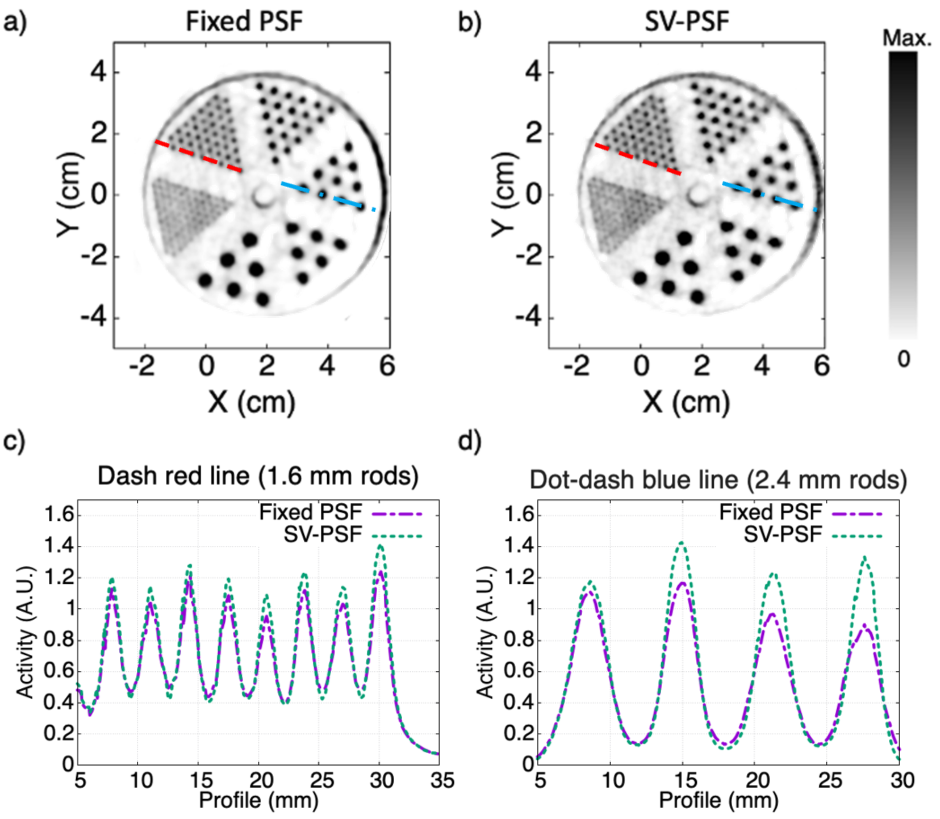

Figure 9: Reconstruction whith a) fixed PSF and b) SV-PSF of an off-centered Derenzo acquisition with rod diameters of 1.2, 1.6, 2.4, 3.2, 4.0, 4.8 mm. c) Line profiles of the red dashed line for both reconstructions and d) line profiles of the blue dot-dashed line for both reconstructions. All reconstructions have the same noise level in the homogeneous region.

the liver, as it is a relatively large region with quite homogeneous activity distribution. That is, 5 subsets 20 iterations for SV-PSF, and 5 subsets 17 iterations for fixed PSF. The profiles show a clear advantage in resolution for SV-PSF.

Table 2 presents a comprehensive comparison of peak-to-valley ratios (PV) for each mouse heart using both fixed PSF and SV-PSF reconstruction techniques. The PV ratios serve as a metric to evaluate the image resolution quality, specifically capturing the ratio between the maximum intensity within the myocardium and the minimum intensity within the same region.

The results displayed in the table demonstrate notable differences between the two reconstruction methods. For Mouse 1, the PV ratio is 3.86 with fixed PSF, while SV-PSF achieves a significantly higher PV ratio of 5.97. Similarly, Mouse 2 exhibits a PV ratio of 2.79 with fixed PSF, which increases to 3.52 with SV-PSF. Mouse 3 follows a similar trend, with a PV ratio of 2.64 for fixed PSF and 3.91 for SV-PSF. Mouse 4 shows a PV ratio of 4.10 with fixed PSF, whereas SV-PSF achieves a higher PV ratio of 6.02.

The observations from this table, combined with the profiles depicted in figure 12,

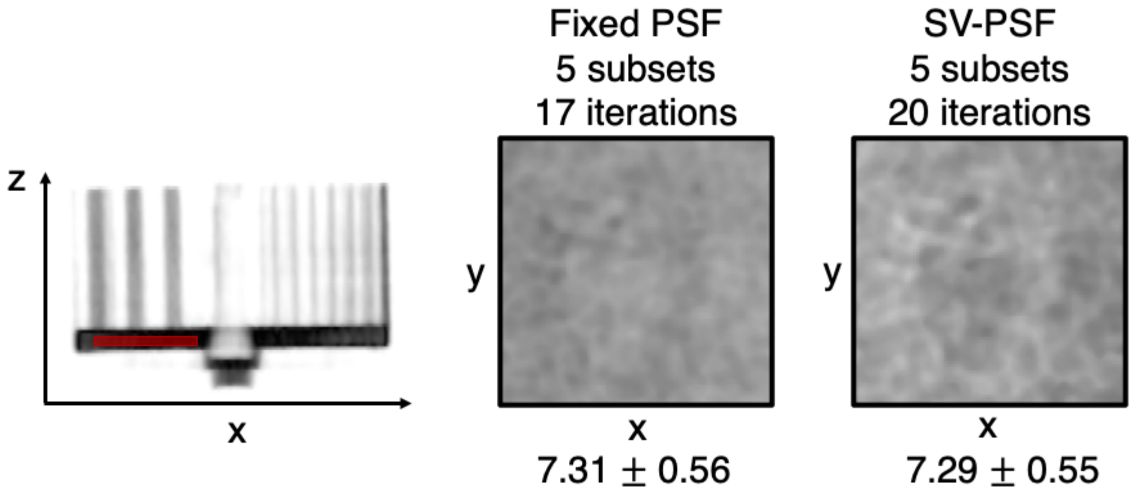

Figure 10: Comparison of Fixed PSF and SV-PSF Reconstructions at Equivalent Noise Levels. The figure depicts a Derenzo phantom with a ROI exhibiting homogeneous activity, highlighted in red on the left. On the right, two ROIs are displayed, one reconstructed using fixed-PSF and the other using SV-PSF reconstruction, both stopped at the same noise level. The bottom of each panel showcases the mean and standard deviation values for the respective ROIs, with Fixed PSF yielding 7.31 ± 0.56 and SV-PSF resulting in 7.29 ± 0.55.

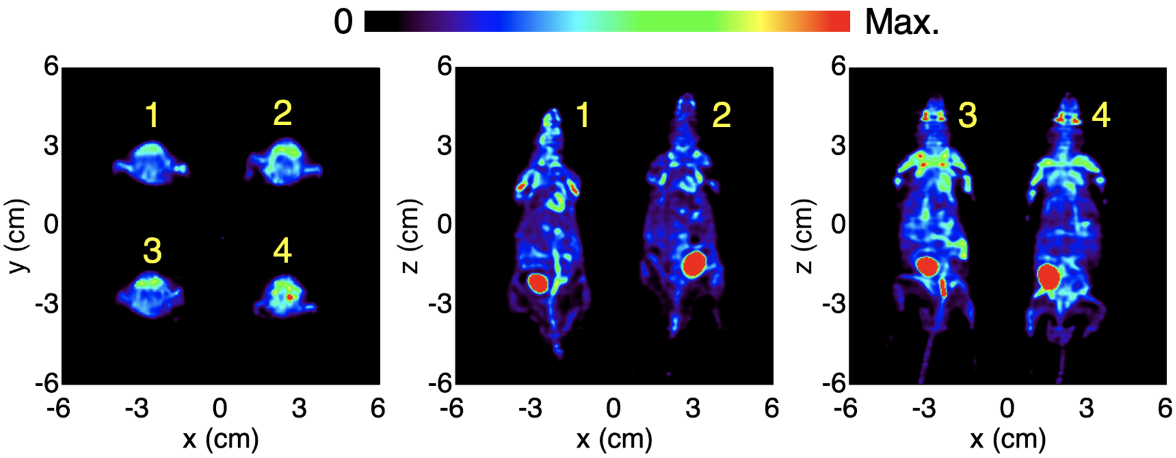

Figure 11: Reconstruction with SV-PSF of a simultaneous acquitision of four mice. Transverse view with the four mice (left), coronal view with mice 1 and 2 (middle), and coronal view with mice 3 and 4 (right). The heart regions for every mouse are shown in figure 12.

clearly demonstrate that SV-PSF reconstruction consistently yields higher PV ratios compared to fixed PSF. These results emphasize the improved resolution achieved through SV-PSF, across the whole FOV, enhancing image quality and capturing finer

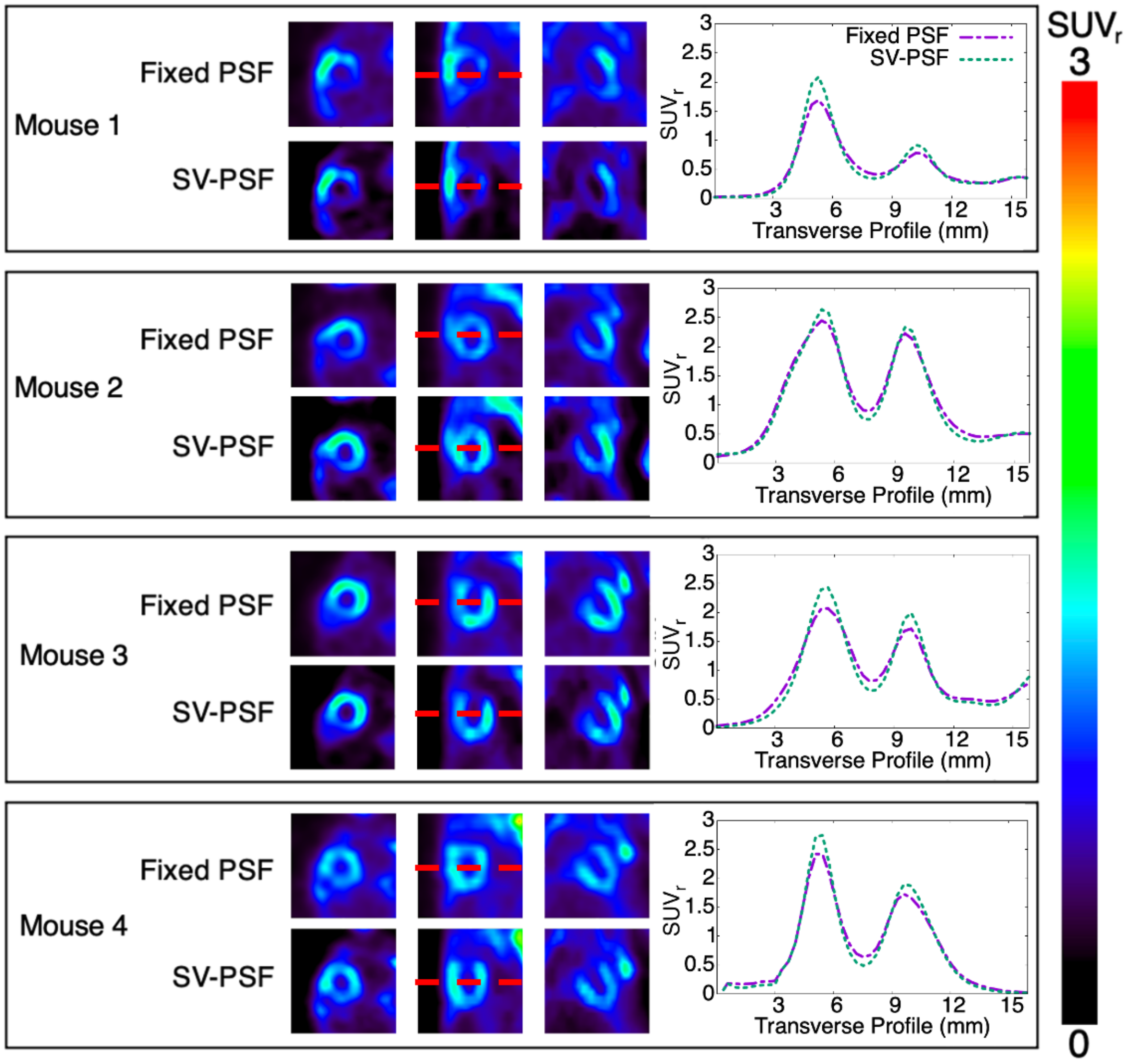

Figure 12: Comparison of four mice heart reconstructions using fixed PSF and SV-PSF in the transverse, sagittal and coronal views. The activity of each heart is presented as relative standard uptake value (SUV_r) normalized to the whole heart. Four mice were acquired simultaneously in the FOV. Transverse profile comparisons are shown on the right. Both fixed PSF and SV-PSF images are shown at an equivalent noise level measured in the bladder.

details within the myocardium of the four mice.

3.5. Benchmark

Figure 13 illustrates the computational time required for a single iteration of image reconstruction. The reconstruction process involved 301x301x195 voxel images obtained from a list file containing 400,000 counts, which is typically equivalent to one second of acquisition in a preclinical study of four mice using the 4R-SuperArgus system. The

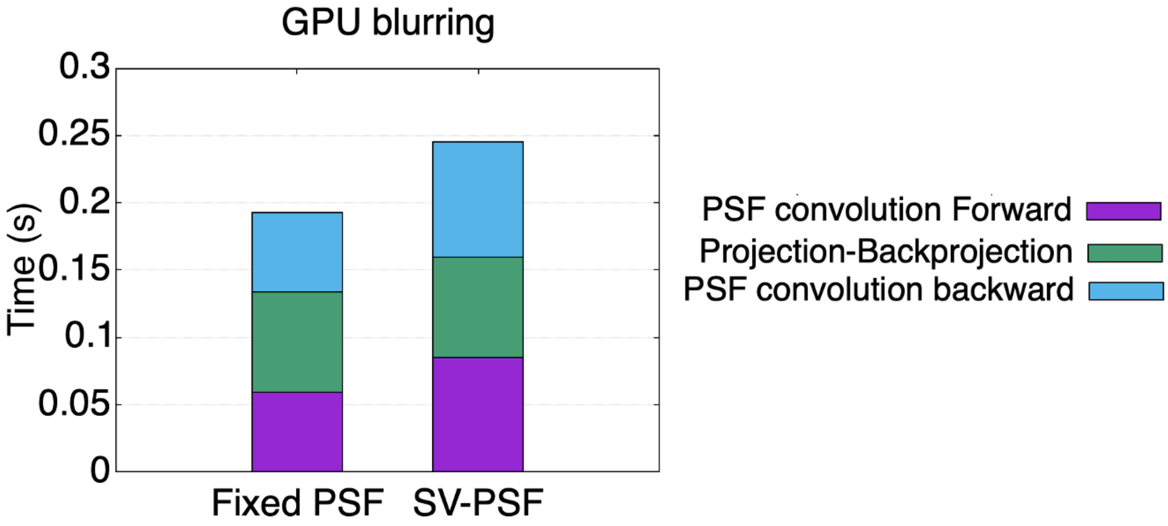

Figure 13: Comparison of computational time per iteration for the reconstruction of 400,000 counts on a Quadro GV100 GPU for the fixed PSF and SV-PSF algorithms. The iteration consists of two blurring processes and a projection-backprojection step, for a reconstructed image of 301x301x195 voxels.

reconstructions were performed using an Intel(R) Xeon(R) W-2155 CPU (3.3 GHz, up to 4.5 GHz in turbo mode) and an NVIDIA GPU Quadro GV100.

Both fixed PSF and SV-PSF methods exhibited similar forward and backward projection times. However, the application of the PSF blurring kernel took almost twice as long for the SV-PSF method, contributing significantly to the overall reconstruction time (70% in this case). Despite this, the total time per iteration for the SV-PSF method remained below 0.25 seconds, just 25% larger than for the Fixed PSF case. This enabled near real-time reconstructions of four iterations, each corresponding to one second of data, making it suitable for real-time image tracking.

In comparison, the Fixed PSF method achieved a slightly higher iteration rate of five iterations per second under the same conditions. However, considering the considerable improvement in resolution demonstrated by the SV-PSF method in this study, the marginal difference in iteration speed is justified. The findings suggest that real-time reconstruction using the SV-PSF method is now achievable, offering the potential to obtain high-quality images with improved resolution within a reasonable reconstruction time.

4. Discussion and conclusions

The iterative reconstruction technique using a GPU with a spatially variant resolution model was implemented on 4R-SuperArgus and 6R-SuperArgus scanners. The SV-PSF was estimated from a simulated grid of point sources inside the FOV of the scanner at discrete positions that is interpolated during reconstruction. These simulations were validated against real point source acquisitions in certain positions (see table 1), achieving maximum differences of 5%. We used 3D gaussians with different widths in the radial, tangential and axial directions to parameterized the SV-PSF.

In the MC reconstruction, the projection and backprojection steps of the iterative algorithm are performed using a full MC simulation which takes into account most of the physical processes involved in PET. Since the MC reconstruction attempts resolution recovery without any approximation to the geometry or the physics of the problem, we have used it as a gold standard for image quality comparisons. Despite its potential, MC reconstruction is not widely used since it is very time consuming. Figure 8 shows that the SV-PSF described in section 2.3 performed almost as well as the gold standard MC reconstruction with much less computational effort.

In figure 9, the use of the SV-PSF model results in a noticeable improvement in the visual quality of the Derenzo phantom, particularly for bars located farther from the center. The line profiles further demonstrate superior resolution for all bars, with an 8% reduction in FWHM for the 1.6 mm rods compared to the Fixed PSF method. More significantly, the SV-PSF model achieves a remarkable 23% reduction in FWHM for the 3 mm rods situated away from the center. Similarly, in figure 12, the use of SV-PSF yields better definition of the myocardium in mice. This improvement is quantified in Table 2, where the SV-PSF model demonstrates a significant capacity for achieving higher PV ratios. This enhancement has important implications for quantification in functional multi-animal studies and the identification of small lesions, as the PV ratio improves by 26% to 55%.

It is worth noting that different factors impact the PV ratio in comparison to the FWHM metric of the Derenzo rods. While both the Derenzo phantom and myocardium exhibit improvements with the SV-PSF model, the influence of background activity differs between the two cases. In the case of the Derenzo phantom, where no background activity is present, the fixed-PSF method aligns closer to the FWHM values obtained by the SV-PSF. On the other hand, for the myocardium, the SV-PSF model demonstrates even greater disparity with the fixed-PSF, highlighting its superior performance in the presence of background activity.

The present study proposes a novel approach to address the issue of spatial resolution variation in PET imaging caused by DOI. Unlike previous approaches, such as dividing the crystal into bins [37], our method has a minimal impact on reconstruction time, enabling real-time imaging.

It is important to note that the SV-PSF method proposed does not take into account positron range. This is because the range of ^{18}F is not highly relevant in this context. Furthermore, positron range is dependent on the tissue and cannot be generalized for every patient. In cases where a high-range isotope is used, such as ^{124}I, ^{82}Rb, or ^{68}Ga, we recommend implementing a specific positron range correction kernel, as proposed in previous works [14, 33, 38].

SV-PSF reconstructions will also be highly beneficial in unrestrained awake animal imaging [39, 40]. In this type of reconstructions, the same organ, such as the brain, will be positioned across different places in the FOV, thus achieving homogeneous resolution in the whole FOV is of paramount importance.

This study focuses on achieving optimal spatial homogeneity while maintaining the same noise levels in fixed-PSF images. Although the homogeneity of noise has not been thoroughly investigated in our method, SV PSF may not only provide superior spatial uniformity, but also improved noise texture across the field of view, leading to increased detectability [41]. Further research, utilizing various phantoms and conducting more in-depth noise analysis, is necessary to validate this hypothesis.

5. Acknowledgments

We acknowledge support by the Spanish Government (PID2021-126998OB-I00, RTC2019-007112-1 XPHASE-LASER, CPP 2021-008751 NEWMBI), as well as European Regional and Resilience Funds, and the European Union's Horizon 2020 research and innovation programme. We also acknowledge support from Instituto de Salud Carlos III (PT20/00044), Comunidad de Madrid (S2022/BMD-7403-RENIM-CM) P. G. also acknowledges support from the Margarita Salas Fellowship, CT18/22 at Complutense University of Madrid funded by the European Union-Next-GenerationUE funds. J. L. H also acknowledges support from Project PDC2022-133057-I00 funded by MCIN/AEI /10.13039/501100011033 and the European Union Next Generation EU/ PRTR.

References

[1] Cheng, Tee E. ; Yoder, Karmen K. ; Normandin, Marc D. ; Risacher, Shannon L. ; Converse, Alexander K. ; Hampel, Joseph A. ; Miller, Michael A. ; Morris, Evan D.: A rat head holder for simultaneous scanning of two rats in small animal PET scanners: Design, construction, feasibility testing and kinetic validation. In: Journal of Neuroscience Methods 176 (2009), jan, Nr. 1, 24–33. http://dx.doi.org/10.1016/j.jneumeth.2008.08.031. – DOI 10.1016/j.jneumeth.2008.08.031. – ISSN 01650270

[2] Greenwood, Hannah E. ; Nyitrai, Zoltan ; Mocsai, Gabor ; Hobor, Sandor ; Witney, Timothy H.: High-Throughput PET/CT Imaging Using a Multiple-Mouse Imaging System. In: Journal of Nuclear Medicine 61 (2020), feb, Nr. 2, 292–297. http://dx.doi.org/10.2967/jnumed.119.228692. – DOI 10.2967/jnumed.119.228692. – ISSN 0161–5505

[3] Kang, Kyung J. ; Oh, Se J. ; Nam, Kyung R. ; Ahn, Heesu ; Park, Ji-Ae ; Lee, Kyo C. ; Choi, Jae Y.: Validation of Image Qualities of a Novel Four-Mice Bed PET System as an Oncological and Neurological Analysis Tool. In: Journal of Imaging 7 (2021), feb, Nr. 3, 43. http://dx.doi.org/10.3390/jimaging7030043. – DOI 10.3390/jimaging7030043. – ISSN 2313–433X

[4] Amirrashedi, Mahsa ; Zaidi, Habib ; Ay, Mohammad R.: Towards quantitative small-animal imaging on hybrid PET/CT and PET/MRI systems. In: Clinical and Translational Imaging 8 (2020), aug, Nr. 4, 243–263. http://dx.doi.org/10.1007/s40336-020-00376-y. – DOI 10.1007/s40336–020–00376–y. – ISSN 2281–5872

[5] Prasad, Rameshwar ; Zaidi, Habib: Scatter Characterization and Correction for Simultaneous Multiple Small-Animal PET Imaging. In: Molecular Imaging and Biology 16 (2014), apr, Nr. 2, 199–209. http://dx.doi.org/10.1007/s11307-013-0683-2. – DOI 10.1007/s11307–013–0683–2. – ISSN 1536–1632

[6] Efthimiou, Nikos ; Wright, John D. ; Clayton, Luke ; Renard, Isaline ; Zagni, Federico ; Caribé, Paulo R. ; Archibald, Stephen J. ; Cawthorne, Christopher J.: Influence of multiple animal scanning on image quality for the Sedecal SuperArgus2R preclinical PET scanner. In: Frontiers in Physics 8 (2021), S. 531662

[7] Mumcuoglu, E.U. ; Leahy, R. ; Cherry, S.R. ; Zhou, Zhenyu: Fast gradient-based methods for Bayesian reconstruction of transmission and emission PET images. In: IEEE Transactions on Medical Imaging 13 (1994), Nr. 4, S. 687–701. http://dx.doi.org/10.1109/42.363099. – DOI 10.1109/42.363099

[8] Qi, Jinyi ; Leahy, Richard M. ; Cherry, Simon R. ; Chatziioannou, Arion ; Farquhar, Thomas H.: High-resolution 3D Bayesian image reconstruction using the microPET small-animal scanner. In: Physics in Medicine and Biology 43 (1998),

apr, Nr. 4, 1001–1013. http://dx.doi.org/10.1088/0031-9155/43/4/027. – DOI 10.1088/0031–9155/43/4/027

[9] Herraiz, J L. ; España, S ; Vaquero, J J. ; Desco, M ; Udías, J M.: FIRST: Fast Iterative Reconstruction Software for (PET) tomography. In: Physics in Medicine and Biology 51 (2006), aug, Nr. 18, 4547–4565. http://dx.doi.org/10.1088/0031-9155/51/18/007. – DOI 10.1088/0031–9155/51/18/007

[10] Gong, Kuang ; Kim, Kyungsang ; Cui, Jianan ; Wu, Dufan ; Li, Quanzheng: The Evolution of Image Reconstruction in PET. In: PET Clinics 16 (2021), oct, Nr. 4, 533–542. http://dx.doi.org/10.1016/j.cpet.2021.06.004. – DOI 10.1016/j.cpet.2021.06.004. – ISSN 15568598

[11] Qi, Jinyi ; Leahy, Richard M.: Iterative reconstruction techniques in emission computed tomography. In: Physics in Medicine and Biology 51 (2006), jul, Nr. 15, R541–R578. http://dx.doi.org/10.1088/0031-9155/51/15/r01. – DOI 10.1088/0031–9155/51/15/r01

[12] Iriarte, Ana ; Marabini, Roberto ; Matej, Samuel ; Sorzano, Carlos Oscar S. ; Lewitt, Robert M.: System models for PET statistical iterative reconstruction: A review. In: Computerized medical imaging and graphics : the official journal of the Computerized Medical Imaging Society 48 (2016), S. 30–48

[13] Reader, A.J. ; Julyan, P.J. ; Williams, H. ; Hastings, D.L. ; Zweit, J.: EM algorithm system modeling by image-space techniques for PET reconstruction. In: IEEE Transactions on Nuclear Science 50 (2003), Nr. 5, S. 1392–1397. http://dx.doi.org/10.1109/TNS.2003.817327. – DOI 10.1109/TNS.2003.817327

[14] Kertész, Hunor ; Conti, Maurizio ; Panin, Vladimir ; Cabello, Jorge ; Bharkhada, Deepak ; Beyer, Thomas ; Papp, Laszlo ; Jentzen, Walter ; Cal-Gonzalez, Jacobo ; Herraiz, Joaquín L. ; López-Montes, Alejandro ; Rausch, Ivo: Positron range in combination with point-spread-function correction: an evaluation of different implementations for [124I]-PET imaging. In: EJNMMI Physics 9 (2022), aug, Nr. 1, 56. http://dx.doi.org/10.1186/s40658-022-00482-y. – DOI 10.1186/s40658–022–00482–y. – ISSN 2197–7364

[15] Ashrafinia, Saeed ; Din, Hassan Mohy-ud ; Karakatsanis, Nicolas A. ; Jha, Abhinav K. ; Casey, Michael E. ; Kadrmas, Dan J. ; Rahmim, Arman: Generalized PSF modeling for optimized quantitation in PET imaging. In: Physics in Medicine and Biology 62 (2017), jun, Nr. 12, 5149–5179. http://dx.doi.org/10.1088/1361-6560/aa6911. – DOI 10.1088/1361–6560/aa6911. – ISSN 0031–9155

[16] Pratx, G. ; Chinn, G. ; Olcott, P.D. ; Levin, C.S.: Fast, Accurate and Shift-Varying Line Projections for Iterative Reconstruction Using the GPU. In: IEEE Transactions on Medical Imaging 28 (2009), mar, Nr. 3, 435–445. http://dx.doi.org/10.1109/TMI.2008.2006518. – DOI 10.1109/TMI.2008.2006518. – ISSN 0278–0062

[17] Lee, Kisung ; Kinahan, Paul E. ; Fessler, Jeffrey A. ; Miyaoka, Robert S. ; Janes, Marie ; Lewellen, Tom K.: Pragmatic fully 3D image reconstruction for the MiCES mouse imaging PET scanner. In: Physics in Medicine and Biology 49 (2004), oct, Nr. 19, 4563–4578. http://dx.doi.org/10.1088/0031-9155/49/19/008. – DOI 10.1088/0031–9155/49/19/008. – ISSN 0031–9155

[18] Alessio, Adam M. ; Kinahan, Paul E. ; Lewellen, Thomas K.: Modeling and incorporation of system response functions in 3-D whole body PET. In: IEEE Transactions on Medical Imaging 25 (2006), Nr. 7, S. 828–837. http://dx.doi.org/10.1109/TMI.2006.873222. – DOI 10.1109/TMI.2006.873222. – ISSN 02780062

[19] Panin, V.Y. ; Kehren, F. ; Michel, C. ; Casey, M.: Fully 3-D PET reconstruction with system matrix derived from point source measurements. In: IEEE Transactions on Medical Imaging 25 (2006), jul, Nr. 7, 907–921. http://dx.doi.org/10.1109/TMI.2006.876171. – DOI 10.1109/TMI.2006.876171. – ISSN 0278–0062

[20] Miranda, Alan ; Bertoglio, Daniele ; Glorie, Dorien ; Stroobants, Sigrid ; Staelens, Steven ; Verhaeghe, Jeroen: Validation of a spatially variant resolution model for small animal brain PET studies. In: Biomedical Physics & Engineering Express 6 (2020), jul, Nr. 4, 045001. http://dx.doi.org/10.1088/2057-1976/ab8c13. – DOI 10.1088/2057–1976/ab8c13. – ISSN 2057–1976

[21] Miranda, Alan ; Bertoglio, Daniele ; Stroobants, Sigrid ; Staelens, Steven ; Verhaeghe, Jeroen: Low activity [11 C]raclopride kinetic modeling in the mouse brain using the spatiotemporal kernel method. In: Physics in Medicine & Biology 66 (2021), jun, Nr. 11, 115005. http://dx.doi.org/10.1088/1361-6560/abfbf0. – DOI 10.1088/1361–6560/abfbf0. – ISSN 0031–9155

[22] Cloquet, C ; Sureau, F C. ; Defrise, M ; Van Simaeys, G ; Trotta, N ; Goldman, S: Non-Gaussian space-variant resolution modelling for list-mode reconstruction. In: Physics in Medicine and Biology 55 (2010), sep, Nr. 17, 5045–5066. http://dx.doi.org/10.1088/0031-9155/55/17/011. – DOI 10.1088/0031–9155/55/17/011. – ISSN 0031–9155

[23] Cherry, Simon R. ; Sorenson, James A. ; Phelps, Michael E.: Physics in nuclear medicine e-Book. Elsevier Health Sciences, 2012

[24] Zhang, Long ; Staelens, Steven ; Van Holen, Roel ; De Beenhouwer, Jan ; Verhaeghe, Jeroen ; Kawrakow, Iwan ; Vandenberghe, Stefaan: Fast and memory-efficient Monte Carlo-based image reconstruction for whole-body PET. In: Medical Physics 37 (2010), jun, Nr. 7Part1, 3667–3676. http://dx.doi.org/10.1118/1.3455287. – DOI 10.1118/1.3455287. – ISSN 00942405

[25] Matej, Samuel ; Li, Yusheng ; Panetta, Joseph ; Karp, Joel S. ; Surti, Suleman: Image-Based Modeling of PSF Deformation With Application to Limited Angle PET Data. In: IEEE Transactions on Nuclear Science 63 (2016), oct,

Nr. 5, 2599–2606. http://dx.doi.org/10.1109/TNS.2016.2607019. – DOI 10.1109/TNS.2016.2607019. – ISSN 0018–9499

[26] DESPRÉS, Philippe ; JIA, Xun: A review of GPU-based medical image reconstruction. In: Physica Medica 42 (2017), oct, 76–92. http://dx.doi.org/10.1016/j.ejmp.2017.07.024. – DOI 10.1016/j.ejmp.2017.07.024. – ISSN 11201797

[27] PRATX, Guillem ; XING, Lei: GPU computing in medical physics: A review. In: Medical Physics 38 (2011), may, Nr. 5, 2685–2697. http://dx.doi.org/10.1118/1.3578605. – DOI 10.1118/1.3578605. – ISSN 00942405

[28] KINOUCHI, S ; YAMAYA, T ; YOSHIDA, E ; TASHIMA, H ; KUDO, H ; SUGA, M: GPU implementation of list-mode DRAMA for real-time OpenPET image reconstruction. In: IEEE Nuclear Science Symposuim & Medical Imaging Conference, IEEE, oct 2010. – ISBN 978–1–4244–9106–3, 2273–2276

[29] SZIRMAY-KALOS, László ; KACSÓ, Ágota ; MAGDICS, Milán ; TÓTH, Balázs: Dynamic PET Reconstruction on the GPU. In: Periodica Polytechnica Electrical Engineering and Computer Science 62 (2018), dec, Nr. 4, 134–143. http://dx.doi.org/10.3311/PPee.11739. – DOI 10.3311/PPee.11739. – ISSN 2064–5279

[30] NAGY, Kálmán ; TÓTH, Miklós ; MAJOR, Péter ; PATAY, Gergely ; EGRI, Győző ; HÄGGKVIST, Jenny ; VARRONE, Andrea ; FARDE, Lars ; HALLDIN, Christer ; GULYÁS, Balázs: Performance Evaluation of the Small-Animal nanoScan PET/MRI System. In: Journal of Nuclear Medicine 54 (2013), oct, Nr. 10, 1825–1832. http://dx.doi.org/10.2967/jnumed.112.119065. – DOI 10.2967/jnumed.112.119065. – ISSN 0161–5505

[31] UDIAS, JM ; GUTIERREZ FERNANDEZ, C ; HERRAIZ, JL ; PEREZ-BENITO, D ; GALVE, P ; LOPEZ-MONTES, A ; LOPEZ-LONGAS, J ; ARCO, JM ; DESCO, M ; VAQUERO, JJ: Performance evaluation of the PET subsystem of the extended FOV SuperArgus 6R preclinical scanner. In: Proceedings of the IEEE Nuclear Science Symposium and Medical Imaging Conference, Sydney, Australia, 2018, S. 10–11

[32] SHEPP, L. A. ; VARDI, Y.: Maximum Likelihood Reconstruction for Emission Tomography. In: IEEE Transactions on Medical Imaging 1 (1982), oct, Nr. 2, 113–122. http://dx.doi.org/10.1109/TMI.1982.4307558. – DOI 10.1109/TMI.1982.4307558. – ISSN 0278–0062

[33] CAL-GONZÁLEZ, Jacobo ; PEREZ-LIVA, Mailyn ; HERRAIZ, Joaquin L. ; VAQUERO, Juan J. ; DESCO, Manuel ; UDIAS, Jose M.: Tissue-dependent and spatially-variant positron range correction in 3D PET. In: IEEE transactions on medical imaging 34 (2015), Nr. 11, S. 2394–2403

[34] RUETSCH GREGORY, Massimiliano Fatica a.: CUDA Fortran for Scientists and Engineers. Elsevier, 2014. http://dx.doi.org/10.1016/C2013-0-00006-0. http://dx.doi.org/10.1016/C2013-0-00006-0. – ISBN 9780124169708

[35] GALVE, P. ; ARIAS-VALCAYO, F. ; MONTES, A.L. ; VILLA-ABAUNZA, A. ; IBANEZ, P. ; HERRAIZ, J.L. ; UDÍAS, J.M.: Ultra-fast Monte Carlo PET Reconstructor. In:

16th International Meeting on Fully 3D Image Reconstruction in Radiology and Nuclear Medicine, 2021, 152–6

[36] Derenzo, SE ; Budinger, TF ; Cahoon, JL ; Huesman, RH ; Jackson, HG: High resolution computed tomography of positron emitters. In: IEEE transactions on Nuclear Science 24 (1977), Nr. 1, S. 544–558

[37] Zeng, Tianyi ; Gao, Juan ; Gao, Dongfang ; Kuang, Zhonghua ; Sang, Ziru ; Wang, Xiaohui ; Hu, Lingzhi ; Chen, Qun ; Chu, Xu ; Liang, Dong ; Liu, Xin ; Yang, Yongfeng ; Zheng, Hairong ; Hu, Zhanli: A GPU-accelerated fully 3D OSEM image reconstruction for a high-resolution small animal PET scanner using dual-ended readout detectors. In: Physics in Medicine & Biology 65 (2020), dec, Nr. 24, 245007. `http://dx.doi.org/10.1088/1361-6560/aba6f9`. – DOI 10.1088/1361–6560/aba6f9. – ISSN 0031–9155

[38] Herraiz, Joaquín L ; Bembibre, Adrián ; López-Montes, Alejandro: Deep-learning based positron range correction of PET images. In: Applied sciences 11 (2020), Nr. 1, S. 266

[39] Arias-Valcayo, Fernando ; Herraiz, Joaquín L ; Galve, P ; Vaquero, JJ ; Desco, M ; Udías, José M: Awake preclinical brain PET imaging based on point sources. In: 15th International Meeting on Fully Three-Dimensional Image Reconstruction in Radiology and Nuclear Medicine Bd. 11072 SPIE, 2019, S. 546–550

[40] Miranda, Alan ; Glorie, Dorien ; Bertoglio, Daniele ; Vleugels, Jochen ; De Bruyne, Guido ; Stroobants, Sigrid ; Staelens, Steven ; Verhaeghe, Jeroen: Awake 18F-FDG PET imaging of memantine-induced brain activation and test–retest in freely running mice. In: Journal of Nuclear Medicine 60 (2019), Nr. 6, S. 844–850

[41] Rahmim, Arman ; Tang, Jing: Noise propagation in resolution modeled PET imaging and its impact on detectability. In: Physics in medicine & biology 58 (2013), Nr. 19, S. 6945